NANO LETTERS

pubs.acs.org/NanoLett Letter

Joule-Heating-Synthesized Iodine–Nitrogen Metal-Free Nanofiber for H_2O_2 Electroproduction via a Coordination Microenvironment Regulation Strategy

Yao Hu,[†] Haihui Lan,[†] Qinyuan Hu,[†] Jiaxuan Gong, Liuhong Yang, Zhaoyu Wang, Tianyi Han,* Xingchen Jiao, Dongjian Shi,* Mingqing Chen, Baochun Guo, and Mingliang Du*

Cite This: https://doi.org/10.1021/acs.nanolett.5c02227 Read Online

ACCESS | Metrics & More | Article Recommendations | Supporting Information

ABSTRACT: The increasing demand for hydrogen peroxide (H_2O_2) necessitates greener production methods. In response, we developed an iodine–nitrogen-codoped metal-free carbon catalyst using the coordination microstructure regulation strategy, combined with rapid Joule heating for precise iodine and nitrogen doping. This approach allows precise control over the formation of active iodine–nitrogen coordination sites, significantly enhancing the catalytic performance for H_2O_2 production via the two-electron oxygen reduction reaction. Among the synthesized catalysts, I–N_4 demonstrated superior catalytic activity, achieving a high H_2O_2 selectivity of 90–96% and a production rate of 1265 mg L^{-1} h^{-1} at −0.4 V vs reversible hydrogen electrode. Operando Raman spectroscopy confirmed the dynamic evolution of intermediates during the reaction, while chronoamperometric tests showed long-term stability. This scalable, energy-efficient synthesis method offers significant potential for sustainable energy and environmental applications.

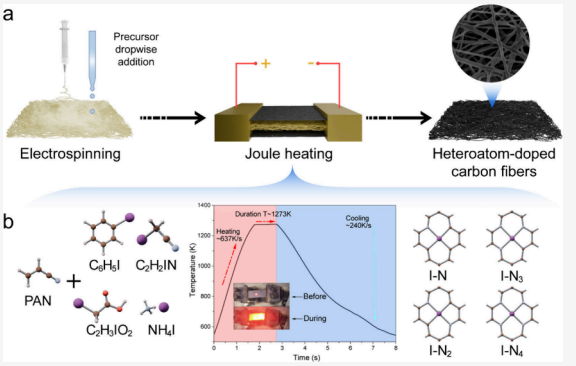

KEYWORDS: *iodine–nitrogen codoping, two-electron oxygen reduction reaction, Joule heating, metal-free catalysis, carbon nanofibers*

The global demand for hydrogen peroxide (H_2O_2) is experiencing steady growth, driven by its widespread use in industries such as paper and pulp, wastewater treatment, and disinfectants.[1,2] In 2024, the H_2O_2 market was valued at USD 3.25 billion and is expected to grow at a compound annual growth rate of over 4%, reaching USD 4.04 billion by 2029.[3] This increase is largely fueled by the rising demand for sustainable packaging, energy storage, and ecofriendly surface disinfectants.[4] Despite its promising growth, the market faces challenges, including high production costs and potential health hazards associated with handling H_2O_2.[5]

The electrochemical synthesis of H_2O_2 is emerging as a promising green alternative to traditional production methods.[6] This approach offers a cleaner, more sustainable solution that addresses the growing demand for H_2O_2, particularly in industries focused on minimizing environmental impacts.[7] However, a key obstacle lies in the thermodynamic favorability of the four-electron ($4e^-$) oxygen reduction reaction (ORR) pathway, which leads to water formation instead of H_2O_2, thereby introducing competitive reaction dynamics.[8] To address this, the development of advanced electrocatalysts that enhance the selectivity of the two-electron ($2e^-$) ORR route and suppress the competing $4e^-$ pathway is crucial.[9,10] Current research primarily focuses on noble metals, transition metals, and their compounds as ORR electrocatalysts.[11] Noble metals like platinum are costly and scarce, limiting their scalability.[12] Transition metals, while more abundant, still suffer from issues such as poor durability, susceptibility to poisoning by reaction intermediates, and challenges with maintaining long-term stability in harsh reaction environments.[13] Moreover, both noble- and transition-metal catalysts often require precise structural control to avoid agglomeration and ensure optimal performance over time.[14]

Metal-free catalysts, particularly carbon materials, have gained attention due to their lower cost, higher stability, and good catalytic performance.[10,15−17] However, a major challenge remains in effectively introducing enough active centers into carbon-based catalysts to promote the selective $2e^-$ pathway for H_2O_2 formation, while minimizing the competing $4e^-$ pathway that produces water.[18] The incorporation of these active sites is crucial for enhancing both the efficiency and selectivity of the $2e^-$ ORR process. As a result, developing methods to precisely control the introduction of

Received: April 17, 2025
Revised: July 7, 2025
Accepted: July 8, 2025

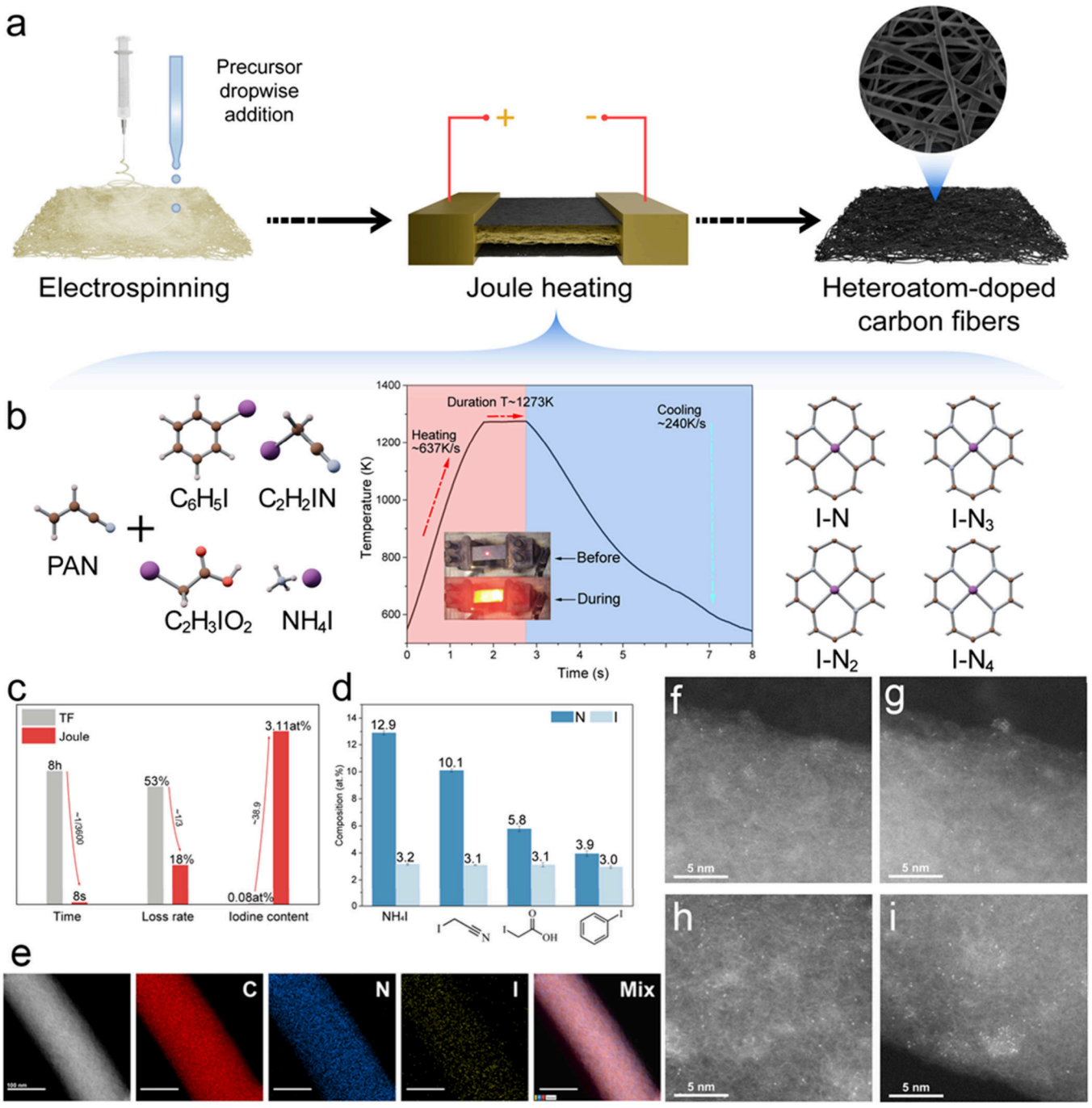

Figure 1. Scheme of the CMR strategy. (a) Electrospinning combined with the Joule heating process flowchart. (b) Formation of different structures from various iodides after Joule heating. (c) Comparison of the time, mass loss rate, and iodine doping content between the Joule heating and tube furnace heating methods. (d) Nitrogen-to-iodine ratio in the Joule-heating synthesis using equimolar amounts of different iodides. (e) STEM elemental mapping images of $I-N_4$. HAADF-STEM images of (f) I–N, (g) $I-N_2$, (h) $I-N_3$, and (i) $I-N_4$.

these reactive centers has become a key focus in advancing the performance of carbon-based catalysts in H_2O_2 production.[1,6]

Herein, we designed iodine–nitrogen metal-free carbon catalysts (IN@MFCs) via a coordination microstructure regulation (CMR) strategy and developed an efficient synthesis method combining electrospinning with Joule heating. Compared to traditional tube furnaces, this approach offers lower energy consumption, reduced material loss, and higher heteroatom loading. By the selection of precursors with tailored coordination environments, precise control over the doping concentration and coordination structure is achieved. The prepared $I-N_4$ catalyst exhibited outstanding activity in 0.1 M perchloric acid under oxygen-saturated conditions, achieving high selectivity (95%) and a low onset potential of −0.785 V vs reversible hydrogen electrode (RHE). At a bias of −0.4 V vs RHE, it achieved a production rate of 1265 mg L^{-1} h^{-1}. Additionally, the $I-N_4$ catalyst maintained stable disk and ring currents, demonstrating approximately 90% selectivity for H_2O_2 over a continuous 10-h electrolysis test. Operando Raman spectroscopy revealed the dynamic evolution of intermediates during the $2e^-$ ORR process, demonstrating the structural integrity of the carbon framework. This strategy

https://doi.org/10.1021/acs.nanolett.5c02227
Nano Lett. XXXX, XXX, XXX−XXX

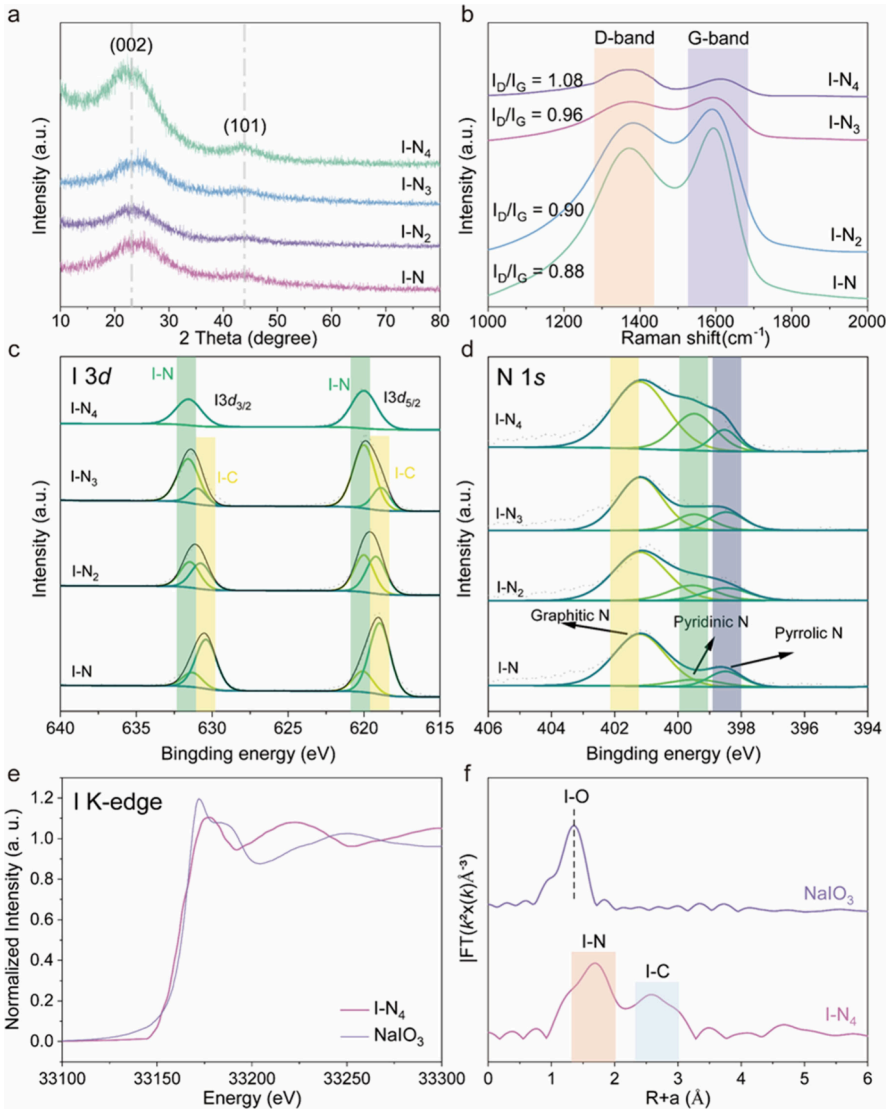

Figure 2. Structural characterization of I–N_4, I–N_3, I–N_2, and I–N. (a) XRD patterns. (b) Raman spectroscopy. (c) XPS survey. (d) I 3d high-resolution spectra. (e) N 1s high-resolution spectra. (e) I K-edge XANES spectra of the I–N_4 sample and $NaIO_3$. (f) EXAFS fitting curve of the I–N_4 sample at *R* space.

enables precise coordination control and enhances durability and catalytic efficiency, offering strong potential for sustainable electrochemical applications.

To develop efficient metal-free catalysts, we designed an iodine–nitrogen-codoped carbon nanofiber catalyst (IN@CNF) via CMR. Combining electrospinning with Joule heating allowed precise control over the heteroatom doping environment. Briefly, ethanol solutions of iodine compounds were added to preoxidized electrospun nanofibers, vacuum-dried, and sandwiched between carbon papers for Joule heating (Figure 1a), significantly enhancing the H_2O_2 electrosynthesis performance. The Joule heating process enables rapid doping and coordination environment optimization. During heating, the temperature rises at ~637 K s^{-1}, holds for 1 s, then cools at ~240 K s^{-1}, completing the entire process in 8 s (Figure 1b). Compared to traditional tube furnace annealing, this method reduces the synthesis time by over 4 orders of magnitude, lowers mass loss by one-third, and increases the iodine doping ratio by 38.9 times (Figure 1c). Using the same precursor, the iodine content in materials produced via a tube furnace is only 0.24%, indicating severe iodine loss (Table S1), whereas materials synthesized by Joule heating retain a significantly higher iodine content of 3.23%. Various iodine compounds served as I and minor N sources, while polyacrylonitrile (PAN)-based electrospun fibers provided the primary nitrogen. Upon heating, both PAN and iodine compounds decompose, forming a nitrogen-doped carbon matrix with effective binding sites for iodine and nitrogen.[19−21] Simultaneously, the iodine compounds decompose, generating reactive species essential for the codoping process. To achieve I–N_4, I–N_3, I–N_2, and I–N coordination structures, we carefully selected ammonium iodide (NH_4I), iodoacetonitrile (ICH_2CN), iodoacetic acid (ICH_2COOH), and iodobenzene (C_6H_5I) as iodine sources for each coordination environment. Joule heating provides extremely high heating and cooling rates, which can prevent extensive atomic diffusion within the material and promote selective coordination with nearby atoms. Rapid cooling, in turn, stabilizes the desired coordination environment by "freezing" it in place.[22−25] Different iodides have distinct

https://doi.org/10.1021/acs.nanolett.5c02227
Nano Lett. XXXX, XXX, XXX−XXX

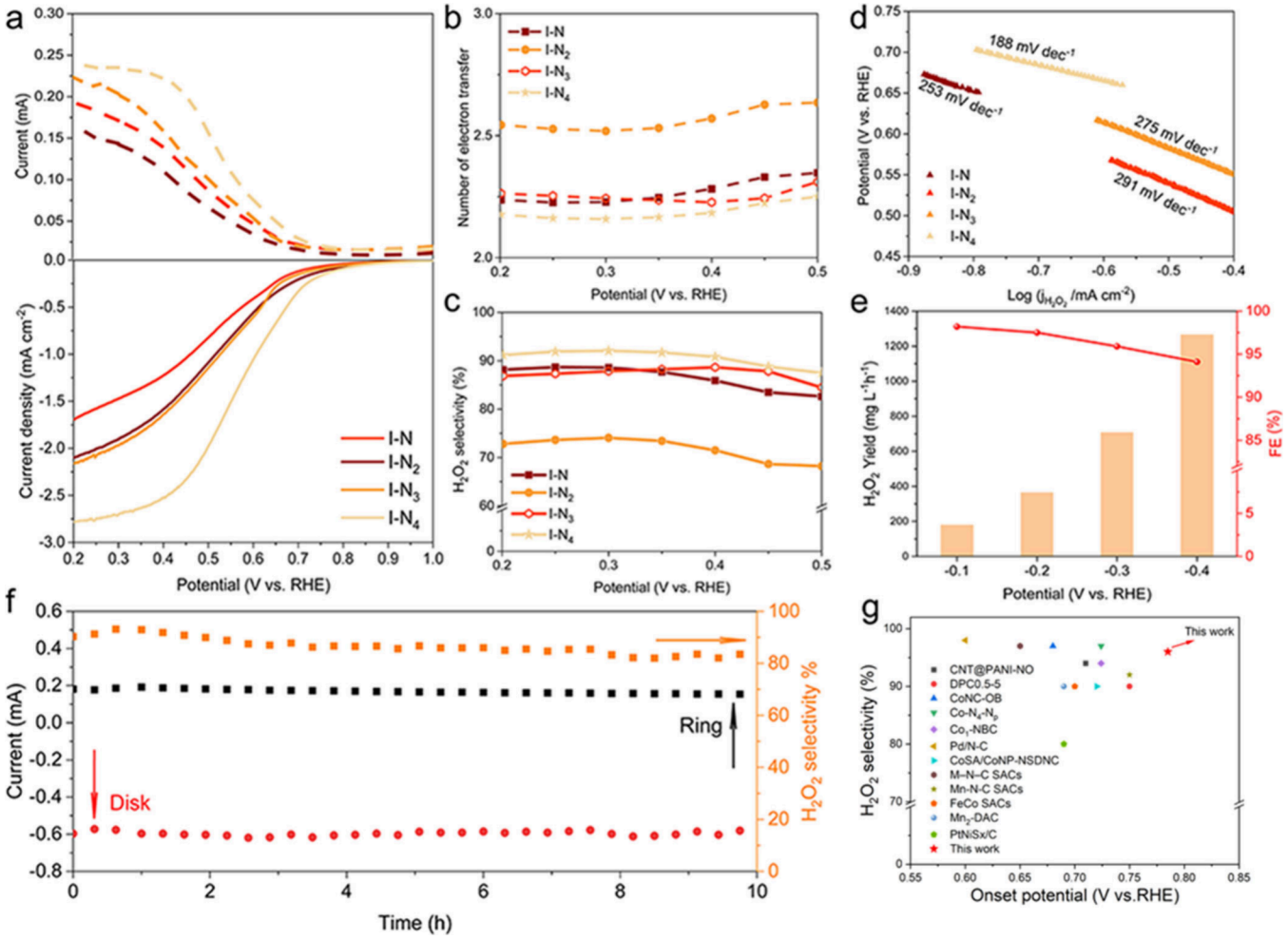

Figure 3. ORR performance of I−N_4, I−N_3, I−N_2, and I−N by RRDE in oxygen-saturated 0.1 M $HClO_4$. (a) LSV curves of all samples at a rotation speed of 1600 rpm and a scan rate of 10 mV s^{-1}. (b) Electron-transfer number for different catalysts calculated from the LSV polarization curves. (c) Molar selectivity of H_2O_2 and (d) Tafel plots of the H_2O_2 current density. (e) H_2O_2 yield of I−N_4 at different potentials and the corresponding Faraday efficiency (FE). (f) Stability assessment of I−N_4. (g) Selectivity and onset potential against the state-of-the-art.

molecular structures and bond energies, which influence their decomposition behavior during Joule heating.[26]

In C_6H_5I, the organic framework shows a strong affinity for carbon,[27] making iodine tend to coordinate with adjacent carbon atoms during heating, forming I−C structures. For ICH_2COOH, the carboxyl group modifies the local environment, enabling iodine to coordinate with either carbon or nitrogen. In ICH_2CN, the nitrile group directs iodine to preferentially bond with nitrogen, forming I−N structures. In NH_4I, iodide ions released during heating exhibit strong nitrogen affinity, promoting highly symmetric I−N coordination. Thus, the local atomic environment critically determines the iodine coordination behavior under Joule heating.

As shown in Figure S1, IN@CNF exhibits uniform carbon nanofibers with diameters of around 150 nm. At the 5 nm scale, HRTEM images (Figure S2) reveal densely arranged graphitized layers with typical sp^2-hybridized stripe-like features, indicating localized graphitization. The SAED pattern shows a diffuse ring without crystalline metal diffraction, confirming the metal-free, carbon-based nature. STEM elemental mapping (Figures 2e and S3−S5) shows uniform atomic-level dispersion of N and I atoms. HAADF-STEM images (Figures 1f−i and S6) suggest that I exists as alternative doping. These results confirm the successful synthesis of I−N_4 structures.

Figure 2a presents the X-ray diffraction (XRD) patterns for I−N_4, I−N_3, I−N_2, and I−N. Two peaks centered at approximately 22 and 44° correspond to the (002) and (101) planes, respectively, of carbon, reflecting the amorphous nature of the matrix. XRD patterns of samples with different iodides show no significant variation, indicating similar average amorphous structures.

The Raman spectrum reveals that the I_D/I_G ratios for I−N_4, I−N_3, I−N_2, and I−N are 1.08, 0.96, 0.90, and 0.88, respectively (Figure 2b). The I_D/I_G ratio of I−N_4 is the highest, indicating the highest defect concentration, which is primarily attributed to the high nitrogen doping level, resulting in a significant increase in disorder within the carbon material.[7,10,28] In contrast, I−N has the lowest I_D/I_G ratio, indicating the highest degree of graphitization and relatively fewer defects.[29,30] As the nitrogen content decreases, the I_D/I_G ratio gradually declines, indicating a reduction in the defect concentration and an increase in the degree of graphitization.[31,32] This trend suggests that, as the nitrogen doping decreases, the carbon framework becomes more ordered and crystalline.[33]

https://doi.org/10.1021/acs.nanolett.5c02227
Nano Lett. XXXX, XXX, XXX−XXX

In the I 3d XPS spectra (Figures 2c and S7), the binding energy peaks of I $3d_{3/2}$ and I $3d_{5/2}$ correspond to the I−N and I−C bonds. Specifically, the I−N bond in I $3d_{3/2}$ is located at 631.5 eV, while the I−C bond is at 630.5 eV; the I−N bond in I $3d_{5/2}$ is located at 620 eV, and the I−C bond is at 619 eV. In I−N_4, the I−N bond peak is the most prominent, indicating that iodine primarily bonds with nitrogen, which is associated with the higher nitrogen doping level in the sample.[34] As the nitrogen doping decreases (as seen in I−N_3 and I−N_2), the I−N bond peak weakens, while the I−C bond peak intensifies, suggesting that iodine increasingly bonds with carbon. In I−N_3, the area percentage of the I−N bond is 71.0%, while that of the I−C bond is 29.0%. In I−N_2, the area percentages of the I−N and I−C bonds are 49.8% and 50.2%, respectively, which are nearly equal. However, in I−N, the I−N bond significantly decreases to 33.1%, while the I−C bond notably increases to 66.9%. Overall, from I−N_4 to I−N, as the nitrogen doping decreases, iodine's bonding tendency gradually shifts from preferentially bonding with nitrogen (I−N bond dominance) to increasingly bonding with carbon (I−C bond dominance). When the nitrogen doping is higher, iodine tends to bond with nitrogen due to nitrogen's higher electronegativity and stronger bond stability. As nitrogen doping decreases, iodine increasingly bonds with carbon, indicating a significant shift in bonding preference, with iodine atoms more readily forming I−C bonds. The ratio of the XPS peak areas clearly supports this change in the iodine's coordination environment. In the N 1s XPS spectra (Figures 2e and S8), the peak of graphitic nitrogen corresponds to a binding energy of 401.2 eV, that of pyrrolic nitrogen is around 399.5 eV, and that of pyridinic nitrogen is approximately 398.5 eV.[35] As the overall nitrogen content decreases, the proportion of graphitic nitrogen increases, indicating a preference for more stable graphitic configurations under low nitrogen doping. Conversely, the proportions of pyridinic and pyrrolic nitrogen decline with higher nitrogen dilution, suggesting that abundant nitrogen promotes the formation of edge- and defect-related nitrogen species. This trend aligns well with the Raman spectroscopy results. In the C 1s XPS spectra (Figures S9 and S10), the C−C bond peak at 284.6 eV dominates across all samples, indicating the most complete carbon backbone structure, which suggests better conductivity. The C−N/I bond appears at 285.8 eV, reflecting significant iodine and nitrogen doping. The C−O bond is observed at 286.4 eV, the C═O bond at 287.2 eV, and the O−C═O bond at 289.5 eV. Overall, the proportion of oxygen-related bonds is low, indicating that the carbon is primarily coordinated with nitrogen and iodine.[36]

The I K-edge X-ray absorption near-edge structure (XANES) and extended X-ray absorption fine structure (EXAFS) spectra provided detailed insights into the coordination environment of iodine in the I−N_4 sample. As shown in Figure 2f, the Fourier-transformed EXAFS spectrum exhibits two distinct peaks at approximately 1.7 and 2.6 Å, corresponding to I−N and I−C coordination, respectively. These features confirm the presence of both I−N and I−C bonds in the local structure. Furthermore, EXAFS fitting and wavelet transform (WT) analysis (Figures S11 and S13 and Table S2) reveal that iodine adopts a 4-fold coordination with nitrogen atoms in the first coordination shell, while carbon atoms are located in the second shell. The simulated EXAFS spectrum based on the I−N_4 structural model also shows excellent agreement with the experimental data (Figure S12), further validating the proposed coordination configuration.

The $2e^-$ ORR performance of the material was evaluated in 0.1 M oxygen-saturated perchloric acid ($HClO_4$). The ORR selectivity and the number of charge transfers were measured using a rotating ring disk electrode (RRDE), all potentials were calibrated to the RHE, and the Pt ring was kept at 1.3 V vs RHE to detect H_2O_2 production. Figure 3a reports the linear-sweep voltammetry (LSV) polarization curve at 1600 rpm. The onset potential of I−N_4 was only 0.785 V vs RHE, indicating its superior catalytic activity for $2e^-$ ORR. At the same time, the selectivity of I−N_4 was maintained at 90−96% in the potential window of 0.6−0.2 V vs RHE, and the number of electron transfers was close to 2 (Figure 3b,c). This is consistent with the theoretical analysis, which predicted a lower reaction energy barrier for the I−N_4 structure, corresponding well with the higher current density observed in the experiments.

The lower nitrogen concentration complicates regulation of the electronic environment around the iodine catalytic center, directly affecting the $2e^-$ ORR. I−N exhibits relatively high current density at higher potentials, and although it is slightly lower than I−N_3 at more negative potentials, its overall performance remains better than than that of I−N_2. The electron-transfer number remains close to 2, indicating that it mainly follows the $2e^-$ pathway to produce H_2O_2. In contrast, I−N_2 has the lowest current density across all potentials. Although it shows relatively good H_2O_2 selectivity at certain potentials, the low nitrogen concentration leads to an overall low current density and significantly reduced catalytic activity. I−N_3, while showing a slightly higher current density than I−N at more negative potentials, has an electron-transfer number consistently above 2.5, and its H_2O_2 selectivity is significantly lower, indicating a preference for the $4e^-$ pathway. In addition, to reveal the nature of the electrocatalytic performance, the Tafel slope was further studied. Based on the Tafel slopes, the catalytic performance follows the order I−N_4 (188 mV dec^{-1}) > I−N (253 mV dec^{-1}) > I−N_3 (275 mV dec^{-1}) > I−N_2 (291 mV dec^{-1}). This indicates that I−N_4 exhibits the best reaction kinetics, followed by I−N and I−N_3, with I−N_2 showing the slowest rate.

Compared to I−N_3, I−N_4 has a higher nitrogen content, enabling more N−C sites to stabilize the iodine center and promote the $2e^-$ pathway for H_2O_2 production. In contrast, the lower N content in I−N_3 limits electronic regulation, favoring the $4e^-$ pathway and reducing selectivity. Despite its low nitrogen level, I−N shows enhanced iodine activity, well-distributed N, and stable coordination, maintaining good selectivity and structural stability. These results suggest that moderate nitrogen doping can be more favorable than excessive doping for optimal catalytic performance.

We conducted chronoamperometric measurements and evaluated the Faradaic efficiency (FE) of I−N_4 in an acidic environment (Figures 3e, S14, and S15). I−N_4 exhibits exceptionally high H_2O_2 FE under a wide potential domain. As the applied potential becomes lower, the FE drops slightly to 94%, which was attributed to the competitive effect of the hydrogen evolution reaction at extreme potentials. At −0.4 V vs RHE, H_2O_2 production using I−N_4 reached 1265 mg L^{-1} h^{-1}. To assess the stability of the catalyst, we performed chronoamperometric tests for I−N_4 at a constant disk potential of 0.63 V vs RHE (Figures 3f and S16). The results demonstrated that I−N_4 maintained stable disk and ring currents, with consistently high H_2O_2 selectivity throughout the continuous electrolysis test. Obviously, I−N_4 exhibits

https://doi.org/10.1021/acs.nanolett.5c02227
Nano Lett. XXXX, XXX, XXX−XXX

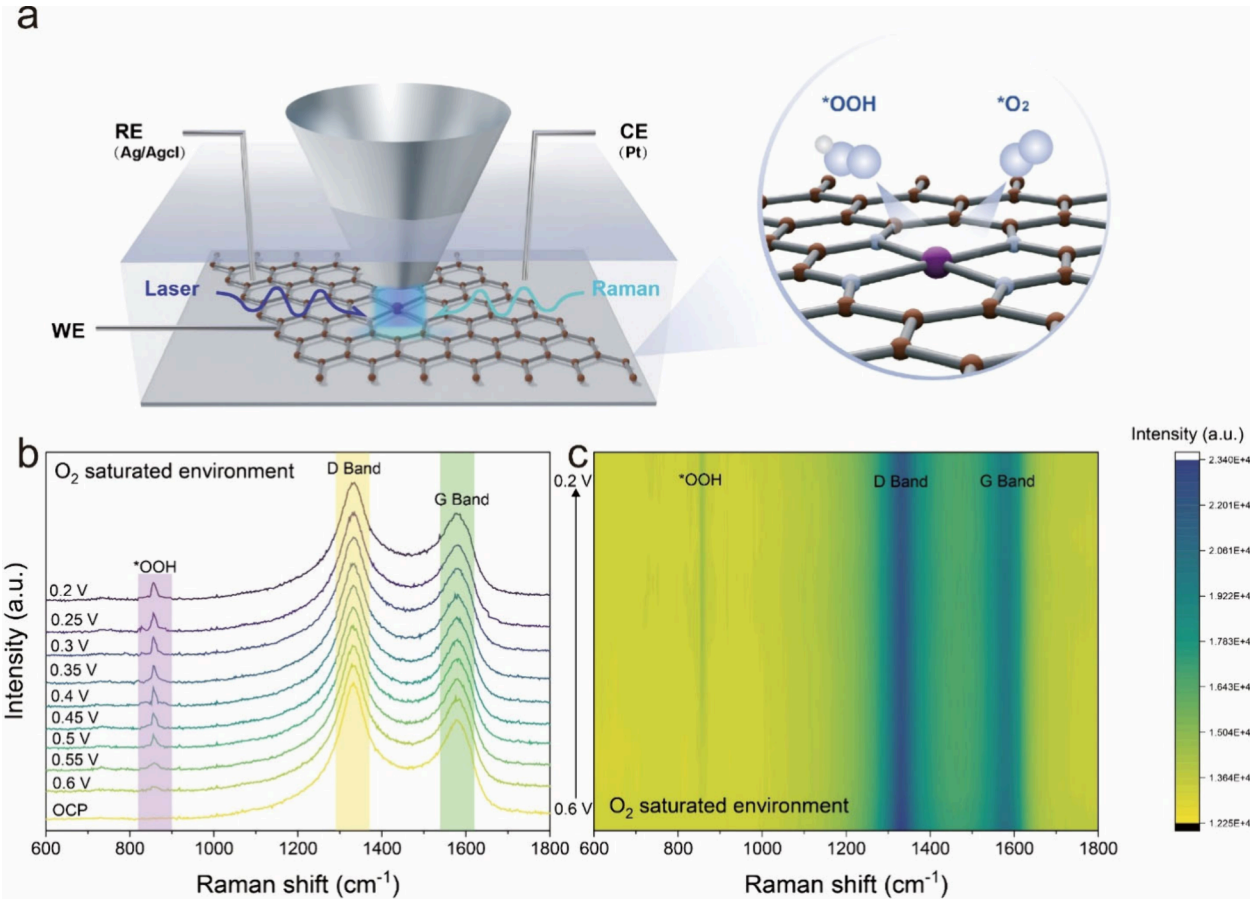

Figure 4. In situ Raman spectra electrochemistry of $2e^-$ ORR based on I−N_4 at different potentials in an oxygen-saturated environment. (a) Scheme of the operando Raman analysis. (b) In situ Raman spectra of $2e^-$ ORR in an oxygen-saturated environment at different potentials. (c) Contour map of in situ Raman spectra on I−N_4.

exceptional ORR catalytic activity and H_2O_2 selectivity in acidic media, surpassing most previously reported catalysts (Figure 3g).

To elucidate the catalytic mechanism, operando Raman spectroscopy was used to monitor the evolution of active sites and interfacial species during $2e^-$ ORR (Figure 4a). In oxygen-saturated conditions, in situ Raman detected a peak at 855 cm^{-1} (Figure 4b,c), attributed to the O−O stretch of the *OOH intermediate. This peak was absent at open-circuit potential but increased and stabilized as the potential decreased from 0.6 to 0.35 V vs RHE, indicating that I−N_4 promotes oxygen adsorption and *OOH formation. No such signal appeared under N_2 (Figure S19). The D and G bands remained stable across all potentials in both atmospheres, confirming the structural integrity of the carbon framework during reaction—essential for long-term stability.

To enhance the accuracy of the synthesis process and to elucidate the underlying reaction mechanisms, density functional theory (DFT) calculations were conducted. As depicted in Figure 5a, tuning of the N content within the nanofibers effectively modulates the local coordination environment surrounding the I catalytic centers. By leveraging the intrinsic electron count differences between N and C atoms, as well as the consequent alterations in symmetry around the I site, this strategy provides precise control over the electronic properties of the active sites.

Changes in coordination environments markedly affect the electronic structure of the I catalytic center. To quantify this, charge density difference maps were calculated for IN@CNF with varying N content (Figure 5b). Increasing adjacent N atoms alters the structural symmetry and local charge distribution. I−N_4 shows the highest symmetry with a distinct 4-fold pattern, while other configurations display lower, typically 2-fold symmetry.

Building on the charge density analysis, the differential bonding behavior was further examined. Iodine tends to form covalent bonds with adjacent carbon, while nitrogen, due to its stable electronic configuration, interacts more weakly with iodine. As the nitrogen content increases, the I p-band center shifts upward, indicating weaker I−atom bonding without significantly raising the system energy. This trend is confirmed by the calculated I p-band centers (Figure 5c), showing a clear increase from I−N to I−N_3. Additionally, the greater electronegativity difference at higher N levels enhances the positive charge on iodine, potentially affecting the catalytic activity.

To quantitatively assess how these structural modifications influence the catalytic performance, we computed the reaction pathway for O_2 reduction to H_2O_2, as shown in Figure 5d. Our computational results reveal that the I−N_4 configuration possesses the lowest energy barrier for the reaction, likely due to its optimized symmetry and effective conjugation with the nanofiber structure, which limits the formation of overly strong covalent bonds with O_2. For the I−N_4 configuration, the primary energy barrier occurs during the adsorption of O_2. Conversely, other configurations exhibit spontaneous O_2

https://doi.org/10.1021/acs.nanolett.5c02227
Nano Lett. XXXX, XXX, XXX−XXX

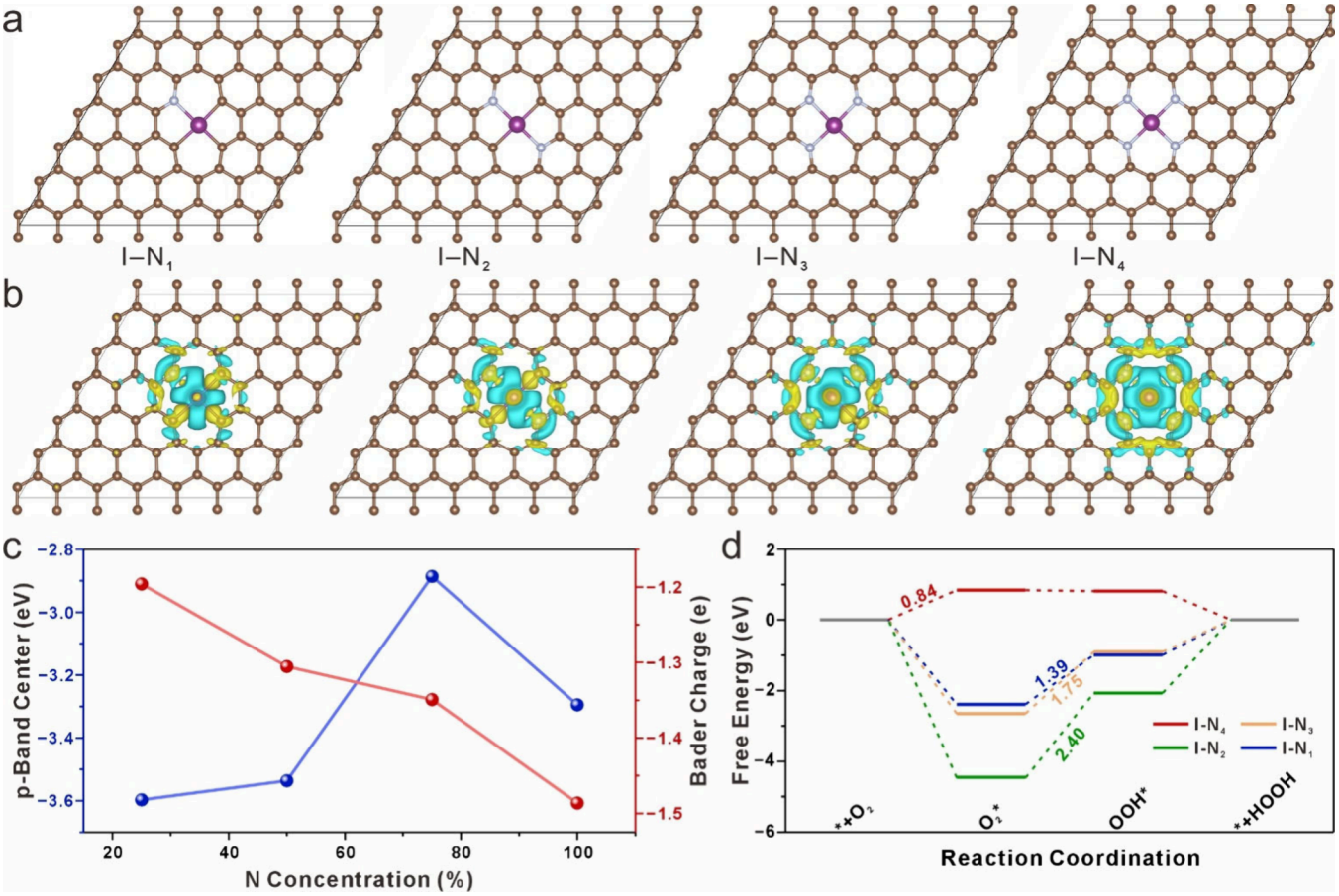

Figure 5. Structural, electronic, and catalytic performances of IN@MFC. (a) Top-view structures of IN@MFC with varying N concentrations. (b) Corresponding charge density difference diagrams, with an isosurface value of 0.003 au. (c) Projected p-band center and Bader charge analysis of I atoms in IN@MFC at different nitrogen concentrations. (d) Free energy profiles of key intermediates for IN@MFC at an applied potential of U = 0.7 V.

adsorption, shifting their rate-limiting step to the subsequent conversion of adsorbed O_2* to OOH*.

The computational findings clearly indicate that the catalytic activity is strongly correlated with the local symmetry and electronic structure, resulting in an activity order of I–N_4 > I–N > I–N_3 > I–N_2. Importantly, this theoretically predicted catalytic trend aligns perfectly with our experimental observations, providing microscopic insights into the catalytic mechanism and further validating the rational design strategy employed. Thus, this combined computational and experimental approach offers a comprehensive understanding of the reaction pathway at the atomic level, ultimately guiding future catalyst optimization.

In summary, we present a versatile and efficient strategy for synthesizing iodine–nitrogen-codoped nanofiber catalysts on carbon nanofibers. By integrating coordination chemistry with rapid Joule heating, this method enables the precise formation of I–N active sites within seconds, avoiding lengthy furnace annealing. The tunable coordination design allows access to multiple configurations, among which I–N_4 shows the highest activity for sustainable H_2O_2 production. This scalable approach holds promise for energy and environmental applications.

■ ASSOCIATED CONTENT

Supporting Information

The Supporting Information is available free of charge at https://pubs.acs.org/doi/10.1021/acs.nanolett.5c02227.

Field-emission TEM images of I–N_3, I–N_2, and I–N, along with STEM elemental mapping images for these samples, details of the relative percentages of iodine, nitrogen, and carbon species in the samples, detection of H_2O_2, and chronoamperometry at different voltages, and microscopic and XRD characterization of I–N_4 after stability testing, as well as in situ Raman spectra of $2e^-$ ORR in a nitrogen-saturated environment at different potentials (PDF)

■ AUTHOR INFORMATION

Corresponding Authors

Tianyi Han – *State Key Laboratory of Tribology in Advanced Equipment, Tsinghua University, Beijing 100084, China;* orcid.org/0000-0001-5908-1851; Email: hanty@mail.tsinghua.edu.cn

Dongjian Shi – *Key Laboratory of Synthetic and Biological Colloids, Ministry of Education, School of Chemical and Material Engineering, Jiangnan University, Wuxi 214122 Jiangsu, China*; Email: djshi@jiangnan.edu.cn

Mingliang Du – *Key Laboratory of Synthetic and Biological Colloids, Ministry of Education, School of Chemical and*

https://doi.org/10.1021/acs.nanolett.5c02227
Nano Lett. XXXX, XXX, XXX–XXX

Material Engineering, Jiangnan University, Wuxi 214122 Jiangsu, China; Zhejiang Provincial Innovation Center of Advanced Textile Technology, Shaoxing 312000, China; orcid.org/0000-0003-2476-8594; Email: du@jiangnan.edu.cn

Authors

Yao Hu − *Key Laboratory of Synthetic and Biological Colloids, Ministry of Education, School of Chemical and Material Engineering, Jiangnan University, Wuxi 214122 Jiangsu, China; Materials Science and Engineering Program & Texas Materials Institute, Walker Department of Mechanical Engineering, The University of Texas at Austin, Austin, Texas 78712, United States;* orcid.org/0009-0005-2042-5895

Haihui Lan − *Department of Chemistry, Massachusetts Institute of Technology, Cambridge, Massachusetts 02139, United States;* orcid.org/0009-0006-1380-1466

Qinyuan Hu − *Key Laboratory of Synthetic and Biological Colloids, Ministry of Education, School of Chemical and Material Engineering, Jiangnan University, Wuxi 214122 Jiangsu, China*

Jiaxuan Gong − *Key Laboratory of Synthetic and Biological Colloids, Ministry of Education, School of Chemical and Material Engineering, Jiangnan University, Wuxi 214122 Jiangsu, China*

Liuhong Yang − *Key Laboratory of Synthetic and Biological Colloids, Ministry of Education, School of Chemical and Material Engineering, Jiangnan University, Wuxi 214122 Jiangsu, China*

Zhaoyu Wang − *Key Laboratory of Synthetic and Biological Colloids, Ministry of Education, School of Chemical and Material Engineering, Jiangnan University, Wuxi 214122 Jiangsu, China*

Xingchen Jiao − *Key Laboratory of Synthetic and Biological Colloids, Ministry of Education, School of Chemical and Material Engineering, Jiangnan University, Wuxi 214122 Jiangsu, China;* orcid.org/0000-0002-5280-9528

Mingqing Chen − *Key Laboratory of Synthetic and Biological Colloids, Ministry of Education, School of Chemical and Material Engineering, Jiangnan University, Wuxi 214122 Jiangsu, China;* orcid.org/0000-0002-4207-8696

Baochun Guo − *Institute of Emergent Elastomers, School of Materials Science and Engineering, South China University of Technology, Guangzhou 510640, China;* orcid.org/0000-0002-4734-1895

Complete contact information is available at: https://pubs.acs.org/10.1021/acs.nanolett.5c02227

Author Contributions

†Y.H., H.L., and Q.H. contributed equally to this work.

Notes

The authors declare no competing financial interest.

■ ACKNOWLEDGMENTS

We thank the National Natural Science Foundation of China (No. 52305198). We are grateful for the technical guidance provided by Lei Cheng from Shenzhen Joule IC Technology Co., Ltd. (http://www.jouleic.com), in utilizing the Joule ultrafast heating device, which significantly contributed to our experimental outcomes.

■ REFERENCES

(1) Deng, Z.; Choi, S. J.; Li, G.; Wang, X. Advancing H_2O_2 Electrosynthesis: Enhancing Electrochemical Systems, Unveiling Emerging Applications, and Seizing Opportunities. *Chem. Soc. Rev.* **2024**, *53*, 8137.

(2) Freese, T.; Meijer, J. T.; Brands, M. B.; Alachouzos, G.; Stuart, M. C. A.; Tarozo, R.; Gerlach, D.; Smits, J.; Rudolf, P.; Reek, J. N. H.; Feringa, B. L. Iron Oxide-Promoted Photochemical Oxygen Reduction to Hydrogen Peroxide (H_2O_2). *EES Catal.* **2024**, *2*, 262.

(3) Qiao, M.; Zhou, X.; Du, Z.; Wu, P.; Zong, B. Chemical and Engineering Bases for Green H_2O_2 Production and Related Oxidation and Ammoximation of Olefins and Analogues. *Natl. Sci. Rev.* **2024**, *11*, nwae243.

(4) Mazzucato, M.; Facchin, A.; Parnigotto, M.; Durante, C. New and Revised Aspects of the Electrochemical Synthesis of Hydrogen Peroxide: From Model Electrocatalytic Systems to Scalable Materials. *ACS Catal.* **2024**, *14*, 6369.

(5) Zheng, Y.; Zhang, Y.; Liang, X.; Ouyang, J.; Guo, X.; Chen, Z. Progress and Opportunities in Photocatalytic, Electrocatalytic, and Photoelectrocatalytic Production of Hydrogen Peroxide Coupled with Biomass Valorization. *ChemSusChem* **2024**, No. e202400472.

(6) Zhang, X.; Gao, D.; Zhu, B.; Cheng, B.; Yu, J.; Yu, H. Enhancing Photocatalytic H_2O_2 Production with Au Co-Catalysts through Electronic Structure Modification. *Nat. Commun.* **2024**, *15*, 3212.

(7) Sun, J.; Chakraborty, J.; Deng, M.; Laemont, A.; Feng, X.; Liu, Y.-Y.; Van Der Voort, P. Metal-Organic Frameworks and Covalent Organic Frameworks as Photocatalysts for H_2O_2 Production from Oxygen and Water. *J. Mater. Chem. A* **2023**, *11*, 21516.

(8) He, H.; Liu, S.; Liu, Y.; Zhou, L.; Wen, H.; Shen, R.; Zhang, H.; Guo, X.; Jiang, J.; Li, B. Review and Perspectives on Carbon-Based Electrocatalysts for the Production of H_2O_2 via Two-Electron Oxygen Reduction. *Green Chem.* **2023**, *25*, 9501.

(9) Yu, A.; Liu, S.; Yang, Y. Recent Advances in Electrosynthesis of H_2O_2 via Two-Electron Oxygen Reduction Reaction. *Chem. Commun.* **2024**, *60*, 5232.

(10) Yang, H.; An, N.; Kang, Z.; Menezes, P. W.; Chen, Z. Understanding Advanced Transition Metal-Based Two Electron Oxygen Reduction Electrocatalysts from the Perspective of Phase Engineering. *Adv. Mater.* **2024**, *36*, 2400140.

(11) Bhoyate, S. D.; Kim, J.; de Souza, F. M.; Lin, J.; Lee, E.; Kumar, A.; Gupta, R. K. Science and Engineering for Non-Noble-Metal-Based Electrocatalysts to Boost Their ORR Performance: A Critical Review. *Coord. Chem. Rev.* **2023**, *474*, 214854.

(12) Wei, Y.; Zhang, W.; Gao, J. Trash or Treasure? Sustainable Noble Metal Recovery. *Green Chem.* **2024**, *26*, 5684.

(13) Yang, H.-M.; Weng, C.-C.; Wang, H.-Y.; Yuan, Z.-Y. Transition Metal Nitride-Based Materials as Efficient Electrocatalysts: Design Strategies and Prospective Applications. *Coord. Chem. Rev.* **2023**, *496*, 215410.

(14) Pei, C.; Chen, S.; Fu, D.; Zhao, Z.-J.; Gong, J. Structured Catalysts and Catalytic Processes: Transport and Reaction Perspectives. *Chem. Rev.* **2024**, *124*, 2955.

(15) Zhai, Q.; Huang, H.; Lawson, T.; Xia, Z.; Giusto, P.; Antonietti, M.; Jaroniec, M.; Chhowalla, M.; Baek, J.-B.; Liu, Y.; Qiao, S.; Dai, L. Recent Advances on Carbon-Based Metal-Free Electrocatalysts for Energy and Chemical Conversions. *Adv. Mater.* **2024**, 2405664.

(16) Deng, B.; Wu, Z. Y.; Feng, E.; Ma, L.; Wang, Z.; Chen, J.; Eddy, L.; Lathem, A.; Wang, T.; Chen, W.; Cheng, Y.; Xu, S.; Liu, Q.; Yakobson, B. I.; Wang, H.; Zhao, Y.; Tour, J. M. Coupling Amorphization and Compositional Optimization of Ternary Metal Phosphides toward High-Performance Electrocatalytic Hydrogen Production. *J. Am. Chem. Soc.* **2025**, *147*, 16129.

(17) Hao, S.; Elgazzar, A.; Zhang, S.-K.; Wi, T.-U.; Chen, F.-Y.; Feng, Y.; Zhu, P.; Wang, H. Acid-Humidified CO_2 Gas Input for Stable Electrochemical CO_2 Reduction Reaction. *Science* **2025**, *388*, 6752.

(18) Chen, K.-Y.; Huang, Y.-X.; Jin, R.-C.; Huang, B.-C. Single Atom Catalysts for Use in the Selective Production of Hydrogen Peroxide

via Two-Electron Oxygen Reduction Reaction: Mechanism, Activity, and Structure Optimization. *Appl. Catal., B* **2023**, *337*, 122987.
(19) Chen, W.; Ge, C.; Li, J. T.; Beckham, J. L.; Yuan, Z.; Wyss, K. M.; Advincula, P. A.; Eddy, L.; Kittrell, C.; Chen, J.; Luong, D. X.; Carter, R. A.; Tour, J. M. Heteroatom-Doped Flash Graphene. *ACS Nano* **2022**, *16*, 6646.
(20) Liu, Y.; Qin, X.; Zhang, S.; Huang, Y.; Kang, F.; Chen, G.; Li, B. Oxygen and Nitrogen Co-Doped Porous Carbon Granules Enabling Dendrite-Free Lithium Metal Anode. *Energy Storage Mater.* **2019**, *18*, 320.
(21) Hu, Y.; Lan, H.; He, J.; Fang, W.; Zhang, W.-D.; Lu, S.; Duan, F.; Du, M. Entropy-Engineered Middle-In Synthesis of Dual Single-Atom Compounds for Nitrate Reduction Reaction. *ACS Nano* **2024**, *18*, 23168.
(22) Chen, Y.; Egan, G. C.; Wan, J.; Zhu, S.; Jacob, R. J.; Zhou, W.; Dai, J.; Wang, Y.; Danner, V. A.; Yao, Y.; Fu, K.; Wang, Y.; Bao, W.; Li, T.; Zachariah, M. R.; Hu, L. Ultra-Fast Self-Assembly and Stabilization of Reactive Nanoparticles in Reduced Graphene Oxide Films. *Nat. Commun.* **2016**, *7*, 1.
(23) Yao, Y.; Huang, Z.; Xie, P.; Lacey, S. D.; Jacob, R. J.; Xie, H.; Chen, F.; Nie, A.; Pu, T.; Rehwoldt, M.; Yu, D.; Zachariah, M. R.; Wang, C.; Shahbazian-Yassar, R.; Li, J.; Hu, L. Carbothermal Shock Synthesis of High-Entropy-Alloy Nanoparticles. *Science* **2018**, *359*, 1489.
(24) Yao, Y.; Huang, Z.; Hughes, L. A.; Gao, J.; Li, T.; Morris, D.; Zeltmann, S. E.; Savitzky, B. H.; Ophus, C.; Finfrock, Y. Z.; Dong, Q.; Jiao, M.; Mao, Y.; Chi, M.; Zhang, P.; Li, J.; Minor, A. M.; Shahbazian-Yassar, R.; Hu, L. Extreme Mixing in Nanoscale Transition Metal Alloys. *Matter* **2021**, *4*, 2340.
(25) Yao, Y.; Huang, Z.; Xie, P.; Wu, L.; Ma, L.; Li, T.; Pang, Z.; Jiao, M.; Liang, Z.; Gao, J.; He, Y.; Kline, D. J.; Zachariah, M. R.; Wang, C.; Lu, J.; Wu, T.; Li, T.; Wang, C.; Shahbazian-Yassar, R.; Hu, L. High Temperature Shockwave Stabilized Single Atoms. *Nat. Nanotechnol.* **2019**, *14*, 851.
(26) Shi, W.; Li, Z.; Gong, Z.; Liang, Z.; Liu, H.; Han, Y. C.; Niu, H.; Song, B.; Chi, X.; Zhou, J.; Wang, H.; Xia, B. Y.; Yao, Y.; Tian, Z. Q. Transient and General Synthesis of High-Density and Ultrasmall Nanoparticles on Two-Dimensional Porous Carbon via Coordinated Carbothermal Shock. *Nat. Commun.* **2023**, *14*, 2294.
(27) Trokowski, R.; Akine, S.; Nabeshima, T. Remarkably Selective Recognition of Iodobenzene Derivatives by a Macrocyclic Bis-Pt II Metallohost. *Chem. - A Eur. J.* **2011**, *17*, 14420.
(28) Luo, Q.; Wang, K.; Zhang, Q.; Ding, W.; Wang, R.; Li, L.; Peng, S.; Ji, D.; Qin, X. Tailoring Single-Atom Coordination Environments in Carbon Nanofibers via Flash Heating for Highly Efficient Bifunctional Oxygen Electrocatalysis. *Angew. Chem.* **2025**, *137*, No. e202413369.
(29) Zhang, B.; Zhang, J.; Hua, M.; Wan, Q.; Su, Z.; Tan, X.; Liu, L.; Zhang, F.; Chen, G.; Tan, D.; Cheng, X.; Han, B.; Zheng, L.; Mo, G. Highly Electrocatalytic Ethylene Production from CO_2 on Nano-defective Cu Nanosheets. *J. Am. Chem. Soc.* **2020**, *142*, 13606.
(30) Xu, F.; Feng, B.; Shen, Z.; Chen, Y.; Jiao, L.; Zhang, Y.; Tian, J.; Zhang, J.; Wang, X.; Yang, L.; Wu, Q.; Hu, Z. Oxygen-Bridged Cu Binuclear Sites for Efficient Electrocatalytic CO_2 Reduction to Ethanol at Ultralow Overpotential. *J. Am. Chem. Soc.* **2024**, *146*, 9365.
(31) Gan, G.; Fan, S.; Li, X.; Wang, J.; Bai, C.; Guo, X.; Tade, M.; Liu, S. Nature of Intrinsic Defects in Carbon Materials for Electrochemical Dechlorination of 1,2-Dichloroethane to Ethylene. *ACS Catal.* **2021**, *11*, 14284.
(32) Ammar, M. R.; Galy, N.; Rouzaud, J. N.; Toulhoat, N.; Vaudey, C. E.; Simon, P.; Moncoffre, N. Characterizing Various Types of Defects in Nuclear Graphite Using Raman Scattering: Heat Treatment, Ion Irradiation and Polishing. *Carbon* **2015**, *95*, 364.
(33) Wang, X.; Jia, Y.; Mao, X.; Zhang, L.; Liu, D.; Song, L.; Yan, X.; Chen, J.; Yang, D.; Zhou, J.; Wang, K.; Du, A.; Yao, X. A Directional Synthesis for Topological Defect in Carbon. *Chem.* **2020**, *6*, 2009.
(34) Liu, J.; Wang, D.; Huang, K.; Dong, J.; Liao, J.; Dai, S.; Tang, X.; Yan, M.; Gong, H.; Liu, J.; Gong, Z.; Liu, R.; Cui, C.; Ye, G.; Zou, X.; Fei, H. Iodine-Doping-Induced Electronic Structure Tuning of Atomic Cobalt for Enhanced Hydrogen Evolution Electrocatalysis. *ACS Nano* **2021**, *15*, 18125.
(35) Li, J. C.; Xiao, F.; Zhong, H.; Li, T.; Xu, M.; Ma, L.; Cheng, M.; Liu, D.; Feng, S.; Shi, Q.; Cheng, H. M.; Liu, C.; Du, D.; Beckman, S. P.; Pan, X.; Lin, Y.; Shao, M. Secondary-Atom-Assisted Synthesis of Single Iron Atoms Anchored on N-Doped Carbon Nanowires for Oxygen Reduction Reaction. *ACS Catal.* **2019**, *9*, 5929.
(36) Hong, J.; Yu, C.; Song, X.; Meng, X.; Huang, H.; Zhao, C.; Han, X.; Wang, Z.; Qiu, J. Theoretical and Experimental Insights into the Effects of Oxygen-Containing Species within CNTs toward Triiodide Reduction. *ACS Sustain. Chem. Eng.* **2019**, *7*, 7527.

https://doi.org/10.1021/acs.nanolett.5c02227
Nano Lett. XXXX, XXX, XXX−XXX